

3D Printing Wireless Connected Objects

VIKRAM IYER, Co-Primary Student Author, University of Washington
JUSTIN CHAN, Co-Primary Student Author, University of Washington
SHYAMNATH GOLLAKOTA, University of Washington

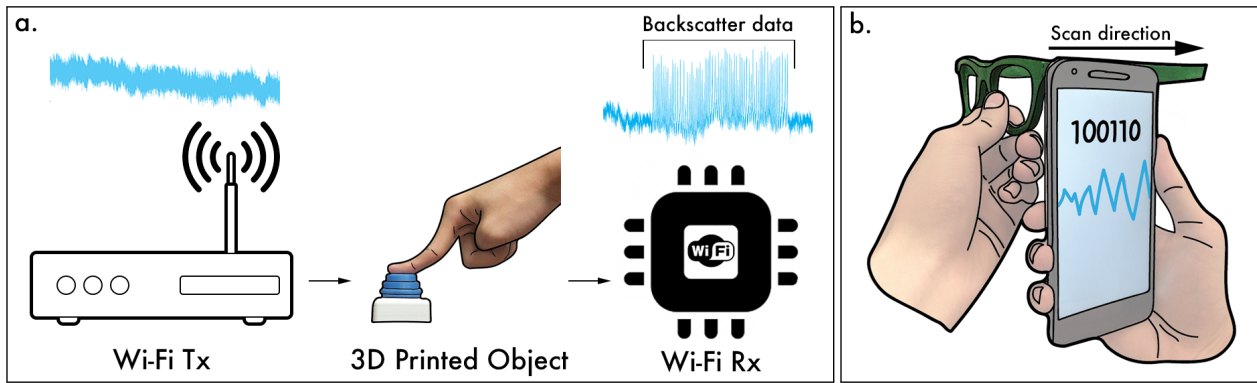


Fig. 1. a) Printed Wi-Fi, the first computational method that sends data to commercial RF receivers including Wi-Fi, enabling 3D printed wireless sensors and input widgets, and b) Printed Maglink, that embeds data within objects using magnetic fields and decodes the data using magnetometers on smartphones.

Our goal is to 3D print wireless sensors, input widgets and objects that can communicate with smartphones and other Wi-Fi devices, without the need for batteries or electronics. To this end, we present a novel toolkit for wireless connectivity that can be integrated with 3D digital models and fabricated using commodity desktop 3D printers and commercially available plastic filament materials. Specifically, we introduce the first computational designs that 1) send data to commercial RF receivers including Wi-Fi, enabling 3D printed wireless sensors and input widgets, and 2) embed data within objects using magnetic fields and decode the data using magnetometers on commodity smartphones. To demonstrate the potential of our techniques, we design the first fully 3D printed wireless sensors including a weight scale, flow sensor and anemometer that can transmit sensor data. Furthermore, we 3D print eyeglass frames, armbands as well as artistic models with embedded magnetic data. Finally, we present various 3D printed application prototypes including buttons, smart sliders and physical knobs that wirelessly control music volume and lights as well as smart bottles that can sense liquid flow and send data to nearby RF devices, without batteries or electronics.

CCS Concepts: • Human-centered computing → Interaction devices;
• Hardware → Sensor devices and platforms;

Additional Key Words and Phrases: Backscatter; Internet of Things

ACM Reference Format:

Vikram Iyer, Justin Chan, and Shyamnath Gollakota. 2017. 3D Printing Wireless Connected Objects. *ACM Trans. Graph.* 36, 6, Article 242 (November 2017), 13 pages. <https://doi.org/10.1145/3130800.3130822>

Permission to make digital or hard copies of all or part of this work for personal or classroom use is granted without fee provided that copies are not made or distributed for profit or commercial advantage and that copies bear this notice and the full citation on the first page. Copyrights for components of this work owned by others than ACM must be honored. Abstracting with credit is permitted. To copy otherwise, or republish, to post on servers or to redistribute to lists, requires prior specific permission and/or a fee. Request permissions from permissions@acm.org.

© 2017 Association for Computing Machinery.
0730-0301/2017/11-ART242 \$15.00
<https://doi.org/10.1145/3130800.3130822>

1 INTRODUCTION

This paper asks the following question: can objects made of plastic materials be connected to smartphones and other Wi-Fi devices, without the need for batteries or electronics? A positive answer would enable a rich ecosystem of “talking objects” 3D printed with commodity plastic filaments that have the ability to sense and interact with their surroundings. Imagine plastic sliders or knobs that can enable rich physical interaction by dynamically sending information to a nearby Wi-Fi receiver to control music volume and lights in a room. This can also transform inventory management where for instance a plastic detergent bottle can self-monitor usage and re-order supplies via a nearby Wi-Fi device.

Such a capability democratizes the vision of ubiquitous connectivity by enabling designers to download and use our computational modules, without requiring the engineering expertise to integrate radio chips and other electronics in their physical creations. Further, as the commoditization of 3D printers continues, such a communication capability opens up the potential for individuals to print highly customized wireless sensors, widgets and objects that are tailored to their individual needs and connected to the Internet ecosystem.

Prior work on computational methods including Infrastuct [Willis and Wilson 2013] and Acoustic Voxels [Li et al. 2016] use Terahertz and acoustic signals to encode data in physical objects, but are limited to embedding static information. We present a novel 3D printing toolkit that not only introduces a new modality for embedding static data using magnetic fields but also enables, for the first time, transmission of dynamic sensing and interaction information via RF signals. Our design can be integrated with 3D digital models and fabricated using commodity desktop 3D printers and commercially available plastic filament materials. Specifically, we introduce two complimentary techniques that 1) send data to nearby



Fig. 2. 3D Printed Wi-Fi Sensors. (a) Anemometer to measure wind speed
(b) Flowmeter to measure water speed (c) Scale to measure weight.

RF receivers (e.g., Wi-Fi) and enable 3D printed wireless sensors and input widgets, and 2) embed static information using magnetic fields on physical objects and decode it using smartphones.

1) Printed Wi-Fi. We present the first 3D printed design that can transmit data to commercial RF receivers including Wi-Fi. Since 3D printing conventional radios would require analog oscillators running at gigahertz frequencies, our design instead leverages Wi-Fi backscatter, which is a recent advance in low-power wireless communication where a device communicates information by modulating its reflection of an incident Wi-Fi signal. The device can toggle an electronic switch to either absorb or reflect an ambient signal to convey a sequence of 0 and 1 bits. The challenge however is that existing Wi-Fi backscatter systems [Kellogg et al. 2016] require multiple electronic components including RF switches that can toggle between reflective and non-reflective states, digital logic that controls the switch to encode the appropriate data as well as a power source/harvester that powers all these electronic components. Our key contribution is to apply Wi-Fi backscatter to 3D geometry and create easy to print wireless devices using commodity 3D printers. To achieve this, we create non-electronic and printable analogues for each of these electronic components using plastic filaments and integrate them into a single computational design. Specifically,

- To print the backscatter hardware, we leverage composite plastic filament materials with conductive properties, such as plastic with copper and graphene fillings. We characterize the RF properties of these filaments and use them to design fully 3D printable antennas and RF backscatter switches (see §3).
- In lieu of digital logic electronics, we encode bits with 3D printed plastic gears. Specifically, ‘0’ and ‘1’ bits are encoded by the presence and absence of tooth on the gear respectively. To backscatter a sequence of bits, the gear teeth are configured to toggle the backscatter switch between reflective and non-reflective states.
- We leverage the mechanical nature of many sensors and widgets to power our backscatter design. We present computational designs that use push buttons to harvest energy from user interaction as well as a combination of circular plastic springs to store energy. Finally, we design 3D printable sensors that directly power the backscatter system, through their sensing operation.

2) Printed MagLink. Our second 3D printed design enables us to embed static information such as the object attributes, its creator



Fig. 3. Printed MagLink objects. Examples of functional and artistic 3D printed objects that are encoded with magnetic fields.

information or version number within 3D printed objects without affecting their appearance. To do this, we look beyond traditional radios such as Wi-Fi and consider other sensing modalities on mobile devices. We note that smartphones today come with magnetometers to aid with navigation. We demonstrate for the first time that one can use smartphone magnetometers to receive data embedded in 3D printed objects. At a high level, to embed a ‘0’ bit we use conventional plastic material and to embed a ‘1’ bit we use ferromagnetic plastic material composed of iron fillings. By varying the material used within a single print job, we can embed multiple sequences of bits across the object. When the user moves her smartphone over the 3D printed object, the magnetic field at the magnetometer changes, which we use to decode bits. Since the object’s color does not affect its magnetic field, our approach can encode information that is visually hidden in the object as shown in Fig. 3. Further, compared to RFID, which provides tagging capabilities but requires a custom expensive reader, our approach enables the information to be read using commodity smartphones.

Achieving this is non-trivial for multiple reasons. First, ferromagnetic materials available for use with 3D printers have very weak magnetic properties compared to magnets. Second, magnetometers are not designed for communication and hence introduce significant noise. For example, in the presence of magnetic fields, the DC bias on the magnetometer significantly changes, interfering with our ability to decode data. Third, users can move the smartphone over the 3D printed objects at different speeds, making it hard to identify symbol boundaries. In §4, we describe encoding and decoding algorithms that address these challenges and enable smartphones to reliably decode data embedded in our 3D printed objects.

We build multiple RF backscatter and magnetic field systems using MakeiT Pro-M, a multi-material consumer-grade 3D printer. Our 3D printed objects backscatter Wi-Fi signals that are then decoded by a receiver. Our evaluation shows that when the Wi-Fi receiver is co-located with the 3D printed object, the RF source can be up to 17 m away or even in a different room and still achieve 16–45 bps with a low bit error rate. We also embed data as magnetic fields on 3D printed objects and use a Nexus 5X smartphone to decode it. Our results show that we can reliably decode data at symbol densities of 1.25 data symbols per centimeter. Further data can be embedded on curved, two- and three-dimensional surfaces.

Finally, we present proof-of-concept 3D printed Wi-Fi sensors, input widgets and smart objects that demonstrate the potential of our 3D printable computational designs. Specifically,

- We design the first fully 3D printed wireless weight scale, flow sensor and anemometer that transmit data via RF signals.

- We design Wi-Fi input widgets including the first button, knob and slider in Fig. 24 that can sense different mechanical motion and send the data to nearby Wi-Fi receivers.
- We finally create two smart objects including a wireless detergent bottle that tracks the amount of detergent used as well as a smart test tube rack for use in a wet lab to tell if a test tube is in the rack.

2 RELATED WORK

Computational fabrication has seen significant advances in printing objects with various functions [Alemanno et al. 2014; Bächer et al. 2016; Koyama et al. 2015; Lau et al. 2011; Pereira et al. 2014; Schüller et al. 2016], computational optimizations [Bickel et al. 2012; Dong et al. 2010; Lan et al. 2013; Mori and Igarashi 2007] as well as the printing process [Gao et al. 2015; Hook et al. 2014; Martínez et al. 2016; Mueller et al. 2014; Optomec 2017; Peng et al. 2016b; Savage et al. 2015a; Schumacher et al. 2015; Wang and Whiting 2016]. Recent work has focused on 3D printing sensors include pneumatic pressure sensors [Vázquez et al. 2015], touch sensors [Schmitz et al. 2015], solenoid motors [Peng et al. 2016a] and hydraulic actuators [MacCurdy et al. 2015]. These sensors are fabricated with modified 3D printers and require a tether to another electronic device for wireless communication. Instead, we introduce computational methods to create wireless sensors that can be fabricated with commercially available 3D printers, and without the aid of additional batteries or electronics. In the rest of this section, we describe the work closely related to printed MagLink and Wi-Fi.

Printed MagLink. 3D watermarking techniques [Uccheddu et al. 2004; Yamazaki et al. 2014; Yeo and Yeung 1999] hide messages by subtly modifying a model’s geometry [Macq et al. 2015]. To extract a message, the printed models have to be scanned back into a digital format and decoded. Smartphone cameras cannot currently be used as decoders as they currently lack the depth resolution to extract an accurate 3D model. In contrast, the magnetic fields produced by our approach can be decoded on commodity smartphones.

Barcodes and QR codes [BarcodeHQ 2017; Hecht 2001] encode information visually and alter an object’s appearance. In contrast, our approach does not alter the exterior of an object since the ferromagnetic material is embedded beneath the object’s surface. Acoustic Voxels [Li et al. 2016] create acoustically resonant structures that can emit musical tones. Printed optics [Willis et al. 2012] uses pipes within objects to direct the flow of light. Acoustic barcodes [Harrison et al. 2012; Savage et al. 2015b] are patterns of physical notches that produce a characteristic sound when plucked with a fingernail. [Chan and Gollakota 2017] manipulates the polarity of magnetized fabric to encode data including 2D images and bit strings.

Finally, while magnetic fields have been used for communication with electromagnets [Jiang et al. 2014; Sun and Akyildiz 2010], we are the first to show that: 1) information can be encoded into objects using 3D printed ferromagnetic material, and 2) smartphones can decode the resulting weak magnetic fields.

Printed Wi-Fi. RFIDs tags that are electronic in nature, require an expensive RFID reader and are designed for tagging and not sensing applications. Chipless RFID designs [Fletcher and Gershenfeld 2000; Fletcher et al. 1996; Preradovic et al. 2009] such as acoustic

wave tags are based on micro-acoustics of piezoelectric crystals instead of semiconductor physics. However these designs have not been demonstrated to be printable on commodity 3D printers. TeraHertz barcode designs including Infrastructs [Willis and Wilson 2013] and [Moshir and Singh 2014] use THz transceivers that are expensive, not commercially available for the average consumer, and unlikely to be integrated with mobile devices in the next few years. Furthermore, all these approaches are limited to encoding static information and cannot enable wireless sensors that require dynamic data communication. In contrast, we enable 3D printed objects that can send dynamic data via RF signals including Wi-Fi, enabling sensors and input widgets without electronics or batteries.

Recent research has made progress towards designing expensive custom printers that can 3D print individual electronic components like capacitors and inductors [Ota et al. 2016; Wu et al. 2015] as well as transistors and diodes [Subramanian et al. 2006; Zebra 2017]. We take a different approach of using commodity printers and designing an electronic-free communication system. Recent work has also demonstrated the ability to 3D print antennas [Adams et al. 2011; Deffenbaugh and Church 2013; Su et al. 2016]. However, none of them create a fully 3D printed communication system. In contrast, we present the first fully 3D printed backscatter system by introducing the first 3D printed backscatter switch, designs for encoding bits as well as mechanisms to power the system.

Finally, ambient backscatter [Kellogg et al. 2014, 2016; Liu et al. 2013; Parks et al. 2014; Wang et al. 2017; Zhang et al. 2016] uses tags with embedded digital logic to modulate an ambient signal like TV, Wi-Fi or FM to convey information. While these tags rely on digital circuits and electronics, our 3D printed computational method eliminates the need for batteries and electronics and demonstrates the ability to design sensors and input widgets that can communicate with Wi-Fi chipsets using only commercial plastic filaments.

3 PRINTED WI-FI

At a high level, the 3D printed object backscatters Wi-Fi signals that can be decoded on wireless receivers. We present our 3D printable backscatter design and the receiver decoding algorithm.

3.1 3D Printed Backscatter Design

Backscatter modulates the radar cross-section of an antenna to encode data in the reflected signal. Backscatter achieves this by switching the impedance of the antenna between two states. 3D printed objects capable of backscattering Wi-Fi signals require multiple components: a 3D printed antenna that can effectively radiate at 2.4 GHz, a 3D printed switch to modulate the antenna impedance and a 3D printed mechanism to encode information.

3.1.1 3D Printed Antennas. We analyze different conductive materials and then present three antenna designs.

Analyzing conductive materials. Designing antennas requires conductive materials capable of passing current in order to radiate EM waves. Commodity 3D printers use fused filament fabrication with nonconductive plastic materials such as acrylonitrile butadiene styrene (ABS) or polylactic acid (PLA). Neither of these is conductive and therefore they cannot be used for 3D printing antennas.

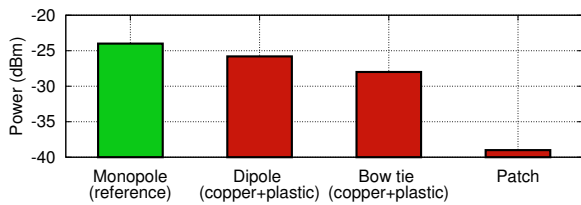


Fig. 4. Comparison of 3D printed antennas. Power received by different antennas from a 2.4 GHz Wi-Fi transmitter in an anechoic chamber.

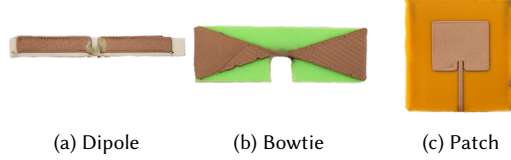


Fig. 5. 3D Printed Antennas

Instead, we explore composite materials that combine conductive materials such as graphene and copper with plastic. Such composite materials have become recently available [All3DP 2017] and further have the advantage of being compatible with commercial 3D printers. The most common conductive filament options are based on graphene and have DC volume resistivities of approximately 0.6 ohm-cm [3d Printing Industry 2017]. A recently developed alternative that combines copper with biodegradable polyester achieves a volume resistivity of 0.006 ohm-cm [Electrifi 2017].

The manufacturers of these materials provide no characterization of their properties at Wi-Fi frequencies (2.4GHz), so prior to designing antennas we evaluate these materials' performance. We fabricate a $50 \text{ ohm } \frac{\lambda}{4}$ microstrip transmission line at this frequency on a 1 mm plastic (PLA) substrate. We then connect the transmission line to standard RF connectors using a colloidal silver paste [Tedpella 2017] and measure its loss using a vector network analyzer (HP8753ES). Our measurements show that copper and graphene based filaments yield a loss of -3 dB and -6.5 dB at 2.45 GHz, respectively; so we choose copper composite filaments.

Dipole. A half-wavelength dipole has many advantages for our 3D printed communication system. At 2.4 GHz, half a wavelength is about 6 cm, making it small enough for easy integration with 3D printed objects. Additionally, dipole antennas have a wide beam width and low directivity allowing flexibility in placement. Fig. 5(a) shows our dipole antenna printed on a 1 mm thick plastic (PLA) substrate with a 2 mm gap between the dipole arms.

Bowtie. A bow tie has a relatively wide beam width and greater bandwidth than a dipole making it more resilient to fabrication error. The bow tie in Fig. 5(b) provides a larger conductive area and as a result a larger reflector for the backscatter signal.

Patch. Patch antennas have the advantage of higher gain than the previous designs and would only radiate outward from the object. As shown in Fig. 5(c), we design a micro strip patch antenna fed by an inset quarter wave transmission line on a 1 mm thick plastic (PLA) substrate over an 55 mm by 70 mm ground plane also made of the same conductive filament. The exact patch width, length and feed inset were modeled and optimized using Ansys HFSS.

To evaluate our 3D printed antenna prototypes, we measure the power received by each antenna from a 2.4 GHz transmitter. We

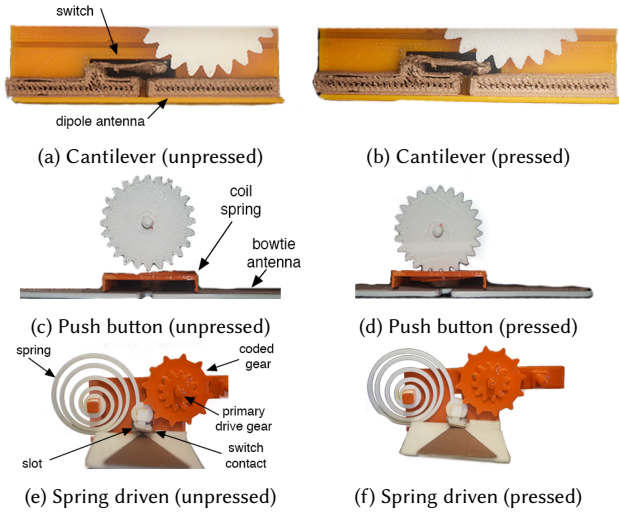


Fig. 6. 3D Printed Backscatter Switches.

conduct the experiment in an anechoic chamber, with the transmitter connected to a conventional monopole antenna placed 2 m away from the antenna under test. Fig. 4 shows that our 3D printed dipole and bow tie receives nearly similar power as an RF monopole antenna. Although a patch antenna should provide the best performance in theory, it performed poorly in our experiments. We suspect this is because our low conductivity materials do not create an effective ground plane. However, our positive results for both the dipole and bowtie demonstrate the first building block of a backscatter system solely with 3D printing.

3.1.2 3D Printed Backscatter Switches. While the antenna serves as the backscatter reflector, the switch provides the means of modulating the antenna between reflective and non-reflective states. A backscatter switch needs to 1) provide a well-defined difference between the two states and 2) enable a short transition between the states by ensuring that the time required to switch is short.

Our 3D printed switch mechanically moves a physical contact made of the same conductive material as our antennas. At a high level, we use the switch to either disconnect or connect the two arms of the antenna. For example, our 3D printed bowtie in Fig. 5(c) has a 2 mm gap between its two halves. The switch either connects the two halves (making the antenna a good RF radiator) or disconnects them. Below, we describe our iterations over three switch designs.

Cantilever Switch. This is composed of a long narrow beam that deforms when pressure is applied. Fig. 6(a) shows the switch integrated with a dipole antenna, as well as a slot in the plastic substrate to allow the switch to move freely. This design relies on the material's stiffness to spring back up to its original state. The rounded contact at the end of the beam connects the two arms of the antenna when pressed as seen in the figure. Fabricating this switch however introduced a few practical complications: First, the length of the cantilever structure is a significant fraction of the wavelength at 2.4 GHz and affects antenna performance. Second, thin structures of the copper composite filament tend to deform when printing due to its lower melting point and stiffness compared to PLA plastic.

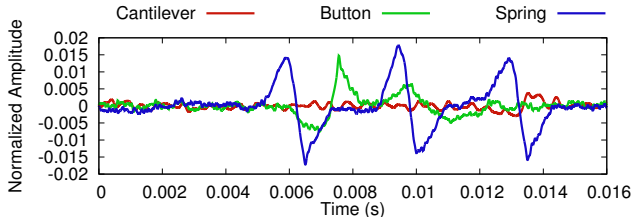


Fig. 7. Comparison of 3D printed switches. The spring driven switch provides a faster response time, large amplitude changes and is consistent.

Printing a thicker beam helped address this, but also increased the amount of force required to actuate the switch.

Push button switch. Our second switch design imitates a push button in Fig. 6(c). Unlike the cantilever design that relies on the stiffness of the beam, a push button requires some sort of separate spring element. We use a planar spring consisting of a 1 mm thick spiral structure where the outer edges of the spiral are fixed to a rectangular case. We also increased the contact area of the switch by 100x which improves the difference in radar cross section.

Spring Driven Switch. Our final switch design builds on the experience of our first two designs as seen in Fig. 6(e). Specifically, we use a planar coil spring orthogonal to the contact surface. This method has the benefits of low force required for actuation as well as a short response time due to the spring. Additionally a slot guides the contact to ensure it stays parallel to the contact surface.

To compare the performance of our switches, we transmit a tone at 2.4 GHz and use an envelope detection circuit to isolate the amplitude changes. Fig. 7 shows that the push button switch provides an 12 dB improvement over the cantilever design. However, the push button bends rather than consistently moves the contact straight up and down. In contrast, our spring driven switch provides a faster response time, large amplitude changes and is consistent. Thus, we choose the spring driven design for our system. We note that springs we printed six months ago still transition the switch cleanly between contact and non-contact states, resulting in clearly decodable backscatter signals. Our experiments (§5.1) involved thousands of switch actuations and we saw no change in the response.

3.1.3 3D Printed Control Logic. The antenna and switch form the basis of a backscatter system, however these elements still require control logic to send a message. We use the teeth of a turning gear to actuate the switch, which then produces a time varying signal. To encode a message using the gears we present two different schemes.

Gear tooth presence. One way of encoding data using gear is to encode a 0 bit by the absence of a tooth and the 1 bit by its presence. An example of this encoding scheme is shown in Fig. 8. To make sure the gear can still interface with others in the system, we stack an additional gear with all of its teeth below the coded gear.

Gear tooth width. An alternative method of encoding information on a gear is to increase the width of the gear teeth themselves. This both increases the amount of time the gear is in contact with the switch, and increases the time between the switch transitions. Fig. 8 shows an alternating pattern of 0 and 1 symbols indicated using the length of the gear. This method has the advantage of not requiring additional synchronization information because information is encoded as differences in time between switch transitions.

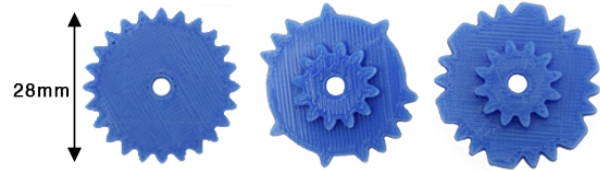


Fig. 8. 3D printed gears. Left: A standard 24 tooth gear with no data encoding. Middle: Coded gear with gear teeth indicating 1 bits and the absence of a tooth indicating a 0 bit. Right: Gear encoded by doubling the teeth width.

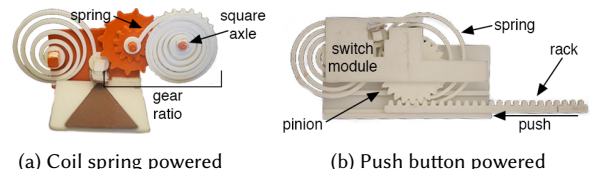


Fig. 9. 3D printed energy storage.

When encoding data spatially on a gear, its circumference determines the length of the message. While gears can be made arbitrarily large, the 3D printed object limits the size. The message size is also affected by the density or spacing of gear teeth. Our results show that we can reliably 3D print involute gears with a circular pitch of 3 mm and pressure angle of 28.

3.1.4 Actuating our 3D Printed Switches. The final element of a backscatter device is an energy storage element used to power the control logic and transmit the message. We present a coil spring that can be wound to store energy. In §6 we show how the 3D printed sensors and input widgets, themselves actuate the control logic.

Coil springs are traditionally used to store mechanical energy in devices such as watches. We use a similar concept to power our control logic. Specifically, we 3D print the tightly coiled planar spring in Fig. 9(a) where the outer edge of the spring is held at a fixed point, and the center is coupled to a gear using a square axle. The spring can be wound up to "charge" the device, and as it unwinds it applies torque to the square axle and therefore the connected gear. Note that we do not attach the coil spring directly to the circular gear encoding bits. Instead, we connect the coil spring to a primary gear shown in the figure, which in turn actuates the circular gear with the encoded bits. By controlling the ratio between the size of the primary and circular gears we can control the speed at which the switch toggles between the two states.

3.2 Printed Wi-Fi Receiver Design

Fig. 10 shows the flowchart for decoding the backscattered information from our printed Wi-Fi objects at the Wi-Fi receiver. At a high level, a Wi-Fi transmitter sends a sequence of Wi-Fi packets and the Wi-Fi receiver uses the changes to the amplitude of the Wi-Fi packets, caused due to the backscatter operation, to extract the backscatter information. In our case, the backscatter signal is a narrowband transmission embedded on top of the ambient Wi-Fi signals, since the printed Wi-Fi objects send data at a low data rate. The Wi-Fi receiver can extract this information by tracking the amplitude of Wi-Fi signals across multiple packets. Specifically, we normalize the received Wi-Fi signals across packets on a scale of +1 to -1 and apply a 10th order 100 Hz low pass filter. This filters

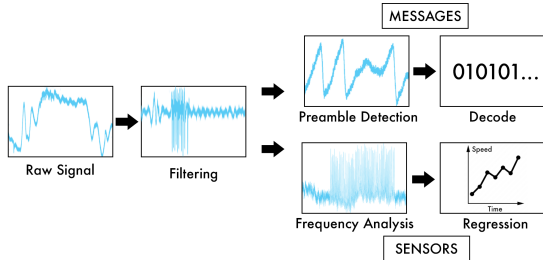


Fig. 10. Printed Wi-Fi processing pipeline.

out the high frequency information in the Wi-Fi signal leaving the backscatter data. Our filter parameters are chosen to minimize noise at bitrates up to 45bps, which is a standard technique in communications. Additionally, our filter bandwidth minimizes the amount of high frequency noise. The resultant data can then be processed for sensing by mapping the sensor value to the rate at which bits are backscattered by the sensor. The backscatter data can also be used to send messages from our input widgets and smart objects. This however requires detecting the beginning of the message, which we achieve using a specific preamble pattern as explained in §6.

We note that prior electronic-based designs use both Wi-Fi signal variations (RSSI) as well as channel state information (CSI) variations [Kellogg et al. 2014] to extract backscatter data. The backscattered signal from our 3D printed objects can be extracted using either of these procedures. Our implementation uses the MAX2829 802.11a/b/g transceiver that gives us access to the received 802.11g baseband signal. So we decode the backscatter information from the amplitude variations in the received Wi-Fi signal across packets.

4 PRINTED MAGLINK

At a high level, by varying the magnetic properties of the material used within a single print job, we can embed multiple sequences of bits across the object. We consider the 3D printed object that modulates the magnetic field as the transmitter and the smartphone magnetometer as the receiver.

4.1 Maglink Transmitter Design

Our data encoding depends on the magnetic properties of the ferromagnetic plastic material used in our 3D printers. Thus, we first analyze its properties and then describe our bit-encoding algorithm.

4.1.1 Analyzing Ferromagnetic Plastic. We use Proto-pasta Magnetic Iron polylactic acid (PLA) which is a compound of Natureworks 4043D PLA and finely ground iron powder [ProtoPasta 2017]. It is a ferromagnetic plastic material that recently comes in filament form for use with 3D printers. Note that the presence of iron particles makes this material ferromagnetic, and so is attracted to magnetic fields. However it is not designed to create permanent magnets. We run a set of experiments to analyze its magnetic properties.

Experimental Analysis 1: Magnetization Curves. When the external magnetic field applied to a ferromagnetic material becomes stronger, its magnetization gradually approaches its *saturation point*. This is when the magnetic domains in the material are aligned in the same direction. To evaluate how the Proto-pasta magnetic Iron PLA material reacts to external magnetic fields, we 3D print a sample toroid shown in Fig. 11(a) using this material and sent it to EMSL

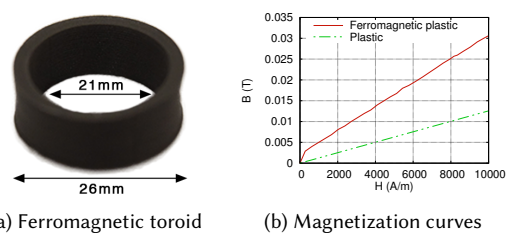


Fig. 11. Magnetic testing. Industrial lab setup for the magnetization curves.

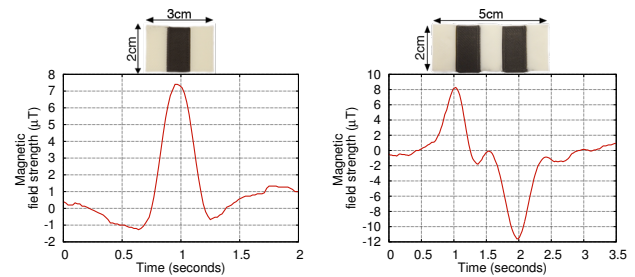


Fig. 12. Encoding mechanisms. a) In the presence/absence of magnetic fields as well as b) polarity. The DC bias is removed.

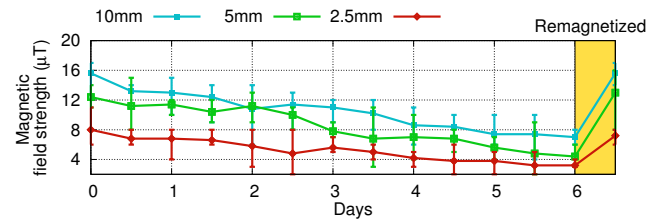


Fig. 13. Magnetic decay over time. We remagnetize the objects in the last time instance and show that they can regain their original field strength.

Analytical, an industrial lab that specializes in material testing and characterization. The lab generated the magnetization curve using the ASTM A596 standard and the Brockhaus model MPG 100 D AC/DC measurement system. A magnetization curve shows the induced magnetic flux density (B) as a function of the magnetic force (H). These curves allow us to quantitatively compare the magnetic properties of our filament to other materials. The results in Fig. 11(b) show that the ferromagnetic filament has a magnetization curve that is slightly larger than that for plastic, making it distinguishable from it. We however note that since our material is magnetically weak, its magnetization curve does not reach the saturation point. In fact, when a magnetic field of 10.000 Am^{-1} was applied to the toroid, the magnetic field strength was 31 mT . The relative permeability ($\mu = \frac{B}{H}$) of our material was measured as 2 Hm^{-1} which translates to a rating of “feebly magnetic”. A 3D printed ferromagnetic cell of dimensions $46 \text{ mm} \times 22 \text{ mm}$ has a field strength of $200 \mu\text{T}$. In contrast a permanent magnet of the same size has a field strength that is at least two orders of magnitude larger. Thus the ferromagnetic plastic material has weak magnetic properties and hence our design should be built to work with feebly magnetic fields.

Experimental Analysis 2: Encoding Schemes. The next question is what kind of a magnetic property can be encoded using these ferromagnetic plastic materials. The key constraint here is that we

need to extract this weak magnetic information from smartphone magnetometers. To this end, we evaluate two ways of encoding.

Presence of magnetic fields. The $22 \times 2 \times 0.5$ cm rectangular strip in Fig. 12(a) is made from a ferromagnetic plastic material (black) and the rest of the object is made from conventional plastic material (white). In order to magnetize the object, we apply a magnetic field using two N45 neodymium magnets of diameter 3.75 mm and thickness of 1.5 mm, separated by a small air gap of 0.5mm. We then move a Nexus 5X smartphone over the 3D printed object which gives magnetic field readings at a rate of 50 Hz. Fig. 12(a) shows the magnetic fields along the x-axis, reported by the magnetometer. The figure shows that we can use the presence and absence of ferromagnetic plastic to encode information on 3D printed objects.

Magnetic Polarity. We print the object in Fig. 12(b) with the black strips made from ferromagnetic plastic material and the white strips made from plastic. To magnetize the object with different polarity, we apply a magnetic field with two N45 neodymium magnets as before but change their polarity. Specifically, for the first strip, we place the north (south) pole of the magnet on the top (bottom) of the strip. While for the second strip, we reverse the order. As before, we swipe the smartphone over the object to record the magnetic field. Fig. 12(b) plots the recorded magnetic field that clearly shows an opposite magnetic field pattern corresponding to the negative polarity. This demonstrates that magnetic polarity can also be used to encode information in our 3D printed objects.

Experimental Analysis 3: Field Strength Decay. A key property of our ferromagnetic material is its *remanence*. Specifically, when the external magnetic field is removed from a ferromagnetic material, the material's magnetization decreases. However, the material still maintains some magnetic remanence. We run experiments to characterize the field strength decay of our magnetized ferromagnetic materials as a function of time. To do this, we 3D print three different rectangular cells of dimensions with lengths 10mm, 5mm and 2.5mm with a width and height of 5mm. We magnetize them by using the procedure described before. We measure the magnetic field as reported by the smartphone, over the course of a week. Fig. 13 shows the results for the three 3D printed objects. Note that $1\text{ }\mu\text{T}$ is the noise floor on the magnetometer and we remagnetize the objects at the end of the week. The figure shows that the large, medium and small magnets lose 55%, 64% and 60% of its original field strength. The key takeaway from these experiments is that the object needs to be remagnetized periodically. Thus, polarity is not suitable for storing data on 3D printed objects. This is because, once the objects loses its magnetic properties, the polarity information cannot be recovered simply by bringing a strong magnet close to the object. This points us to an encoding mechanism where information is encoded in the presence or absence of ferromagnetic material in the object. Specifically, with such an encoding mechanism, we can recover the data simply by bringing a strong magnet close to the object and re-magnetizing the ferromagnetic plastic.

4.1.2 Encoding Procedure. We use the presence and absence of magnetic fields to encode bits – ‘0’ is encoded using convention plastic while a ‘1’ bit is encoded using ferromagnetic plastic material. However since users move the smartphone at different speeds, a

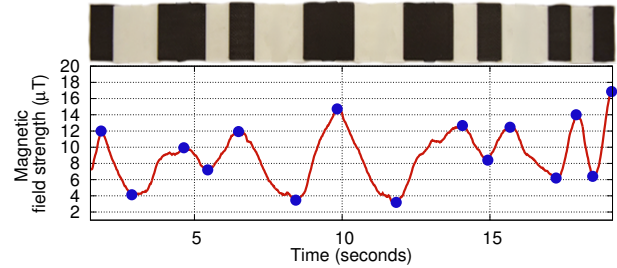


Fig. 14. Decoding a Printed MagLink. For a sequence of ferromagnetic (black) and conventional plastic material (white), we scan a smartphone from left to right. Our decoder yields the code 1011 010111 00.

continuous sequence of 0 or 1 bits can result in the loss of synchronization of symbol boundaries. To prevent this, we encode a ‘0’ bit by a plastic cell followed by a ferromagnetic plastic cell. To encode the ‘1’ bit we use a ferromagnetic plastic cell followed by a plastic cell. This ensures that, within every subsequence of bits, there is a transition from plastic to ferromagnetic plastic and vice versa. All our MagLink tags can be scanned by hand and the encoding/decoding algorithm is designed for variability in hand motion.

Since ferromagnetic material can have the same color as plastic, it is difficult to identify where data is encoded in the object. So, we always encode data starting at the ends of the objects along directions that have smooth edges. If there are smooth surface along multiple directions, we encode data in the vertically increasing direction. For circularly symmetric objects, we can use a sequence of three ferromagnetic cells as our preamble — such a pattern does not occur within data and so the receiver can uniquely identify the beginning, even when the user scans in the opposite direction.

4.2 Maglink Receiver Design

Fig. 14 shows the magnetometer signal for a sequence of magnetic and non-magnetic blocks. The plot highlights two key challenges. First, smartphone magnetometers suffer from a DC bias. In particular, when a magnetic field is applied to the phone, the DC bias can change. Second, there is non-negligible inter-symbol interference as we move the phone from a ferromagnetic plastic cell to a plastic cell and vice versa. This is because the magnetic fields of the adjacent ferromagnetic plastic cell could spill over adjacent cells.

Decoding Procedure. Instead of relying on absolute threshold values, we look for local differences in the magnetic field to decode the information. Specifically, we find the local peaks in the magnetic fields to decode the bits in the 3D printed object. The first step in doing this is to apply smoothing in the form of a moving average to remove the small variances in the signal that result from environmental noise. Our implementation uses a window size of 20 samples. The second step is to find the peaks in the resulting signal. To do this, we run the *IsProminent* function described in Algorithm 1. At a high level the prominence of a peak describes whether it stands out from its neighboring peaks as a result of height and location. A challenge however is that environmental noise can result in spurious peaks which can affect decode. To prevent such peaks, we set the prominence of the desired peaks to 5. This avoids spurious peaks that occur close to the desired peaks. After this we cluster the

Algorithm 1 Maglink decoder

```

1: function DECODE(signal)
2:   smoothed  $\leftarrow$  average(signal)
3:   // locate maximums and minimums
4:   peaks  $\leftarrow$  findpeaks(smoothed)
5:   for peak p in peaks do
6:     if p and p + 1 are closer than 0.1 sec.
7:       or signal hasn't returned to baseline in [p, p + 1]
8:       or !IsProminent(p, minProminence) then
9:         discard p
10:    [shortMax, longMax]  $\leftarrow$  kmeans(maxs in peaks)
11:    [shortMin, longMin]  $\leftarrow$  kmeans(mins in peaks)
12:    sort(shortMax, longMax, shortMin, longMin)
13:    Map symbols to bits
14:
15: function IsPROMINENT(peak, minProminence)
16:   [p1, p2]  $\leftarrow$  highest peak to left/right of peak
17:   [min1, min2]  $\leftarrow$  global min in [p1, peak]/[peak, p2]
18:   prominence  $\leftarrow$  nearest peak above max(min1, min2)
19:   return prominence  $\geq$  minProminence

```

maximums and minimums using the k-means algorithm so we can find clusters of 1 and 2 ferromagnetic and plastic blocks. With this, we can map the symbols to bits where 1 is a maximum followed by a minimum, and a 0 is the inverse.

The advantage of using peaks for decoding instead of thresholds is that they are resilient to DC biases, which in turn can change the threshold values. Moreover, while inter-symbol interference can affect the shape of the recorded signals, we still see a local maximum when the smartphone is in the middle of a ferromagnetic material and a local minimum in the middle of a non-magnetic plastic block.

Our decoder parameters are dependent on the ferromagnetic material and magnetometer. These parameters are a one time calibration on the smartphone app. Magnetic DC offsets from the environment have no effect on our decoder. We rely on relative changes in magnetic field strength. Our system would be affected when a permanent magnet is less than 5 cm from the magnetometer. However, this is not a major concern in practice.

5 EVALUATION

5.1 Evaluating Printed Wi-Fi

To evaluate our design, we first create a prototype printed Wi-Fi object. To do this, we 3D print a bowtie antenna as described in §3.1.1. We shield it with a 2 mm thick layer of PLA plastic to represent plastic casing of an object incorporating printed Wi-Fi. We attach the antenna to the spring driven switch in §3.1.2 to modulate the information backscattered by the object. For our Wi-Fi receiver we use the MAX2829 802.11a/g/b transceiver [Maxim 2004], which outputs the raw received baseband Wi-Fi signal. We connect the transceiver to a 2 dBi gain antenna. We set the transmit power at the Wi-Fi source on channel 11 to 30 dBm and use a 6 dBi antenna, which is within the FCC EIRP limit of 36 dBm.

Operational Range. The range of a Wi-Fi backscatter system is determined by the distance between the Wi-Fi source and printed

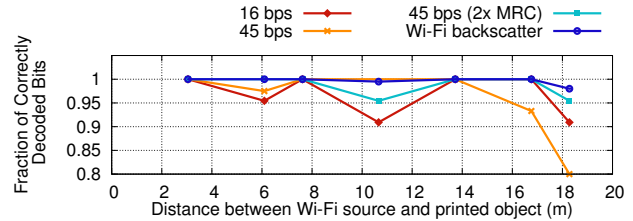


Fig. 15. Range in line of sight scenarios. We vary the distance between the Wi-Fi source and the 3D printed object. We plot the electronic-based Wi-Fi backscatter [Kellogg et al. 2014] as the baseline.

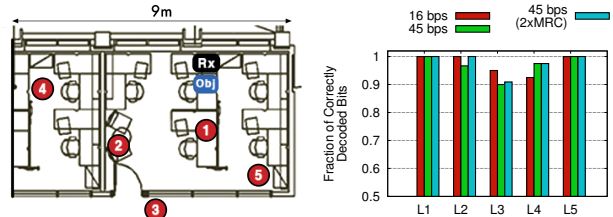


Fig. 16. Testbed setup. The printed Wi-Fi object and Wi-Fi receiver are separated by 15 cm on a table top, and the Wi-Fi source transmitting Wi-Fi packets is tested at five different locations.

Wi-Fi object, and the distance from the printed Wi-Fi object to the wireless receiver [Kellogg et al. 2016]. In our use cases, the user, who carries a Wi-Fi receiver (e.g., smartphone), is close to the 3D printed objects they are interacting with. So, we evaluate the impact of distance between the object and the Wi-Fi source.

Experiments #1. We run experiments in a large 10 by 30 meter room to test the maximum operating range of our system. We fix the distance between the 3D printed object and the wireless receiver to 0.5 m. We then move the Wi-Fi source away from the object along a straight line. To automate the experiments at various distances and preserve consistency, we use a servomotor to rotate the gear a fixed angle and actuate the switch at a constant rate, backscattering a known bit pattern. By changing the speed of the motor, we test bit rates of 16 bps and 45 bps. We note that these bit rates are within the range of what can be achieved by our coil spring in §3.1.4.

Fig. 15 shows the fraction of correctly decoded bits as a function of distance between the Wi-Fi source and 3D printed object. The figure shows the results for two bit rates of 16 bps and 45 bps. The plots show that as expected the number of errors generally increases as the distance between the Wi-Fi source and the 3D printed object increases. We observe certain points with consistent non-monotonic increases in the errors due to multipath in our test environment. To reduce the number of decoding errors, we employ maximum ratio combining (MRC) [Tse and Viswanath 2005] in which we combine the analog signals across two transmissions. The plots show that with MRC, the errors at a bit rate of 45 bps can be significantly reduced. Our results demonstrate that our system is capable of robustly decoding the raw bits. Further, we note that performance can be improved by trading off the length of the transmitted message to employ an error correcting code. For example, the addition of a single parity bit can be used to validate a message and alert the user to retransmit. By further reducing the number of transmitted bits from 24 to 12, we can employ a half rate convolutional code.

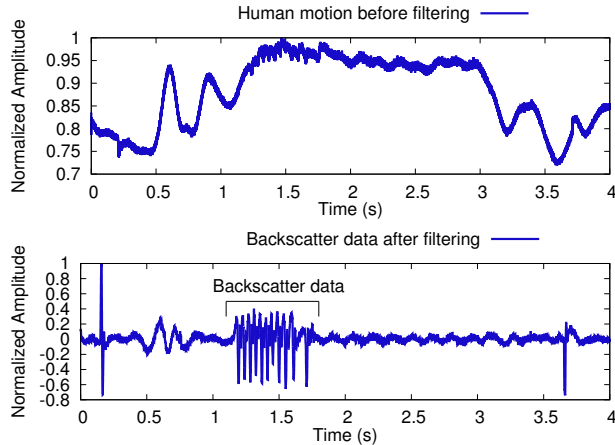


Fig. 17. Backscatter data is decoded by filtering out the human motion.

In the context of a practical use case such as the button, a 12 bit message could still encode 2^{12} unique product identifiers. The key observation from this experiment is that printed Wi-Fi can achieve ranges of up to 17 m from the Wi-Fi source.

In comparison to previous works such as Wi-Fi backscatter [Kellogg et al. 2014] and FS-backscatter [Zhang et al. 2016], we use a higher transmission power of 36 dbm EIRP which corresponds to the FCC limit for transmission power in the 2.4 GHz ISM band. This is the primary reason for why we achieve long ranges in this experiment despite any additional losses incurred in our printed switch. Additionally, we used a 10 by 4 cm bowtie antenna, and a 6 by 1 cm dipole antenna. While still small enough to be incorporated in many printed objects, these are larger than the wearable device scenario evaluated in works such as FS-backscatter. Finally, because it is difficult to compare our range results to the numbers reported in prior work since the evaluation scenarios are different, we replicate the electronic switch and normal monopole antenna using in Wi-Fi backscatter and evaluate it in our deployment. The results are shown in Fig. 15 that show that electronic based Wi-Fi backscatter performs better than our printed Wi-Fi design, which is expected.

Experiments #2. Next, we evaluate our system in non-line of sight scenarios using the testbed shown in Fig. 16. Specifically, we place the backscattering Wi-Fi object and the Wi-Fi receiver on a desk, 15 cm away from each other. We then place the Wi-Fi transmitter in five different locations as shown in the figure. Three of the five locations were in the same room as the 3D printed object while two of the locations were outside the room separated by a double sheet-rock wall with a thickness of approximately 14 cm. We run experiments with the door closed; thus there is no line-of-sight path to the 3D printed object from locations 3 and 4. As before, at each location, we run experiments with two different bit rates of 16 and 45 bps. Fig. 16 shows the fraction of correctly decoded bits as a function of these different locations. The figure shows a high probability close to 1 of correctly receiving a bit when the Wi-Fi transmitter is in the same room as the 3D printed object. As expected, the number of errors increases for 45 bps at location 3 that is outside the room. However at 16 bps, the fraction of correctly

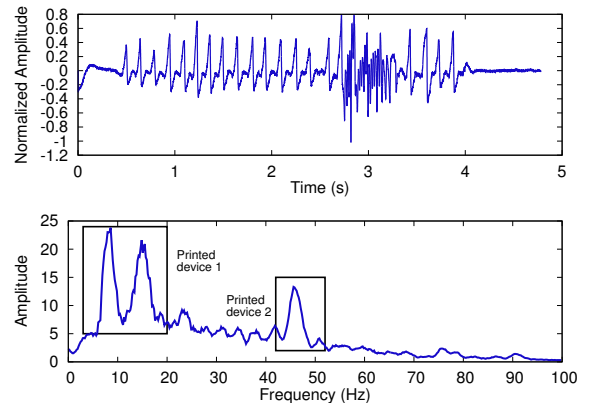


Fig. 18. Multiple printed Wi-Fi devices. The time- and frequency-domain signal in the presence of two objects transmitting at different frequencies.

decoded bits was greater than 0.95. This demonstrates that we can operate even in non-line-of-sight scenarios from the Wi-Fi source.

Effects of Human Motion. Since our printed Wi-Fi system is designed for use with interactive objects, next we evaluate the impact of human motion in close proximity to our backscatter device. We place our Wi-Fi source, backscattering object and Wi-Fi receiver on a tabletop. We use the servomotor to independently turn the gear at 45 bps. At the same time, we make continuous hand gestures between the printed object and Wi-Fi receiver. The raw waveform in Fig. 17 shows the slow variation in the envelope of the received Wi-Fi signal due to human motion. We note that the variation due to human motion is at a significantly lower frequency than an individual switch action, and can be removed when we subtract the moving average. Visually we can see that human motion does not produce the same sharp response that the spring loaded switch is capable of, allowing us to separate them.

Multiple co-located printed Wi-Fi devices. We can enable multiple devices in the same environment by applying standard techniques from wireless communication such as frequency division multiple access (FDMA), code division multiple access (CDMA) or even leveraging spatial multiplexing using multiple antennas [Gollakota et al. 2011]. To perform CDMA, for example, one can configure each 3D printed object to transmit with an orthogonal code by using different patterns of teeth as shown in Fig. 8 to encode different codes. To show that these multiplexing approaches apply directly to our 3D printed objects, we demonstrate the feasibility of multiplexing 3D printed Wi-Fi devices using FDMA.

Specifically, in FDMA, each device operates at a slightly different frequency, which can then be separated at the receiver using band-pass filters. We print two devices with gear ratios that differ by a factor of 4x, which causes them to backscatter at different rates. We place them 70 cm from the transmitter antenna and 20 cm from our receiver antenna. Both devices begin transmitting with an arbitrary time offset without any explicit coordination.

Fig 18 shows the recorded signal in the time-domain, which shows the beginning of the first low rate transmission as well as a short high rate transmission that begins part way through. Fig 18 also shows peaks in the frequency domain corresponding to the two

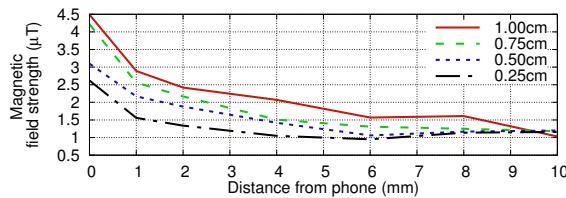


Fig. 19. Magnetic field strength versus distance from phone.

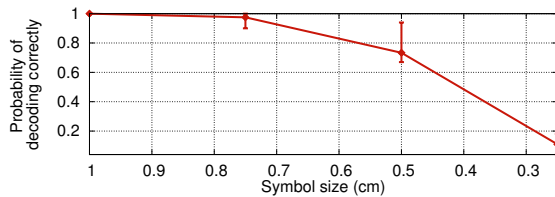


Fig. 20. Bit errors versus symbol size.

devices. The two peaks corresponding to the first device is due to harmonics and imperfections in the fabrication process. To isolate and decode each of these transmissions, we apply a 10th order Butterworth low-pass or high-pass filter with a cut off frequency of 30 Hz. This allows multiple devices to operate in close proximity of each other enabling applications including a single controller with multiple inputs, each of which can transmit data to a Wi-Fi device.

5.2 Evaluating Printed Maglink

Magnetic field strength versus distance. We first measure the magnetic field as a function of distance from the magnetometer. To do this, we 3D print four separate cells of ferromagnetic material with different widths. We magnetize the cells using the procedure described in §4.1. We then swipe each ferromagnetic cell along the x-axis of the smartphone. As described in §4.2, we pass the received signal through a moving average filter to remove extraneous peak values. We measure the average amplitude of peaks reported by the magnetometer. We repeat this experiment for different distances between the magnetometer and the ferromagnetic cells. Fig. 19 plots the average recorded magnetic field as a function of distance for the four ferromagnetic cells. The plots show that as the distance between the smartphone and object increases, the magnetic field strength decreases. Further, the field strength increases with the size of the 3D printed ferromagnetic cell. This is expected because the field strength of a ferromagnet is related to its size. Finally, the average field strength converges at 1 cm at around 1 μT which is the noise floor of our magnetometer. This range is expected because magnetic communication is typically designed for near-fields.

Bit errors versus symbol size. We print four different objects with different symbol densities. Specifically, we change the symbol rate from 1 to 4 symbols/cm by changing the width of the ferromagnetic material. We encode 11 bits on each of these objects. We scan a smartphone across each of the objects at approximately the same speed and measure the BER after passing the magnetometer signal through our decoding algorithm. Fig. 20 shows the BER as a function of the symbol density. The plot shows that as the symbol density increases, the BER increases. This is because of two main reasons. First, at higher symbol densities, the width of the ferromagnetic

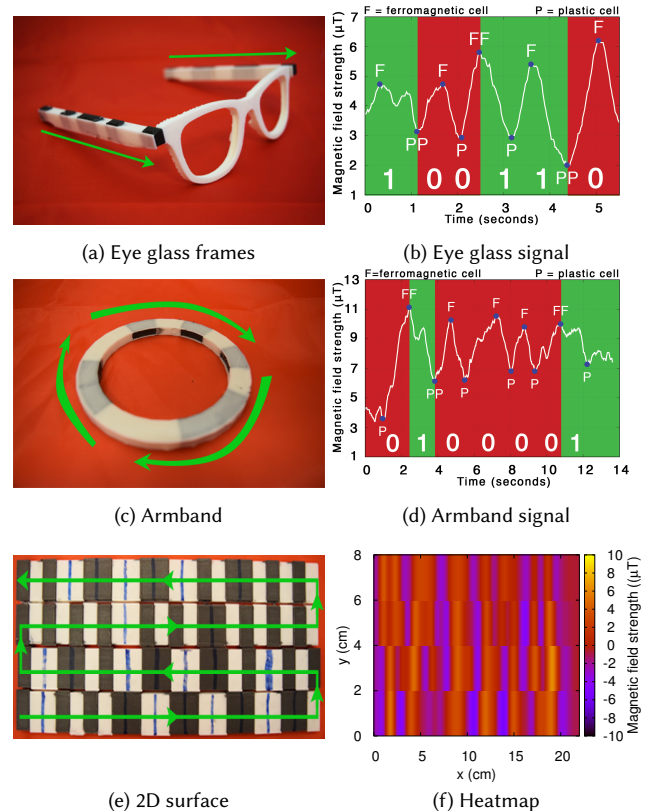


Fig. 21. Encoding and decoding magnetic information on various objects.

material is small and hence the generated magnetic field is weaker, making it difficult to distinguish from a standard plastic material. Second, since we move the phone at approximate the same speed across the objects, there are less magnetometer samples per each symbol making it easier to miss the peaks corresponding to the ferromagnetic material. We can however encode symbols at a density of 1.25 symbols/cm and successfully decode them on a smartphone. **Encoding information in regular objects.** We model and fabricate a pair of eye glass frames with embedded magnetic fields with a symbol length of 1 cm. Fig. 21(a) shows the glasses with data embedded on both arms of the frame, where the black region corresponds to the ferromagnetic material. Given that our frame was 12 cm long, we could encode 6 bits along the length of each arm. This results in 12 bits which is sufficient to encode 2^{12} unique frame types/brands. This information can be read by a smartphone either by scanning on the arm's outer or inner face. The decoded signal at the smartphone from the left arm is shown in Fig. 21(b) showing a strong change in the magnetic field and successful bit decoding. We note that the magnetic field information can be embedded discreetly into the structure of the object by spray-painting it.

Next, to show that our approach works even with curved surfaces, we embed data in the 3D printed armband shown in Fig. 21(c). Our armband has an outside diameter of 9 cm and an inside diameter of 7 cm. We are able to encode 7 bits along the armband. The decoded symbols in Fig. 21(d) show a robust signal that works even on curved surfaces. Finally, we show that we can embed magnetic

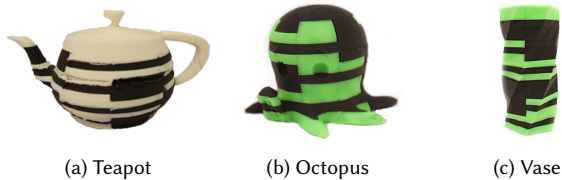


Fig. 22. Embedding data on popular Thingiverse objects. The spray painted versions are shown in Fig. 3.

information as a 2D code shown in Fig. 21(e). 2D codes allow us to embed more bits by covering a larger surface area on the object. We scan the information by moving the smartphone in a zig-zag pattern along the 2D space at an approximately uniform speed. The smallest width of the ferromagnetic material in the figure is 1 cm. Fig. 21(f) shows a heat map of the magnetic field strength as observed by the smartphone magnetometer. Notice that the red peaks in a given layer correspond to the ferromagnetic symbols on the surface. Further, that the width of each red region correspond to the length of the ferromagnetic material. This demonstrates the feasibility of encoding data with magnetic fields on a 2D surface.

Integration with Thingiverse objects. Thingiverse is a popular website for sharing of open-source user created digital design files. To show that our approach can be applied to existing models, we encode data into three popular objects from Thingiverse. We slice the models horizontally at different heights as well as vertically to produce multiple slices. For each slice we print the model either in conventional plastic or in ferromagnetic material, in order to produce a sequence of bits. These bits can be decoded on the smartphone magnetometer by moving it in a vertical motion all around the object. Fig. 22 shows a teapot that encodes 48 bits and an octopus and vase that can each encode 40 bits. Each object is split vertically into 4 or 8 slices and horizontally into anywhere from 11 to 20 layers. Fig. 3 shows the eyeglass, armband, teapot, octopus and vase after spray-painting. We envision that creators can use our technique in this way to create short messages that can be used to attribute ownership or certify authenticity.

We note that the magnetic bits were encoded along mostly uniform surfaces that would be easy to scan. For example we would not encode bits along the handle of the teapot in Fig. 22(a). We combine measurements from all three axes of the magnetometer making the measured signal agnostic to the orientation of the smartphone.

6 WI-FI SENSORS, WIDGETS AND OBJECTS

Wi-Fi sensors. First, we present different 3D printed sensors that can communicate with Wi-Fi receivers using backscatter.

Wireless anemometer. We 3D print a cup anemometer as shown in Fig. 2 to measure wind speeds. The entire setup is sufficiently light that even wind speeds as low as 2.3 m/s will cause it to spin. The hub of the anemometer is attached to backscatter gear that encodes an alternating sequence of zero and one bits. When the hub spins, the backscatter gear pushes against the spring switch. The switch makes contact with the antenna and generates the backscatter signal. Wind speed can be inferred from the rate at which bit transitions occur.

To evaluate our design, we place our 3D printed anemometer 20 cm from our Wi-Fi receiver and place a Wi-Fi source 3 m away.

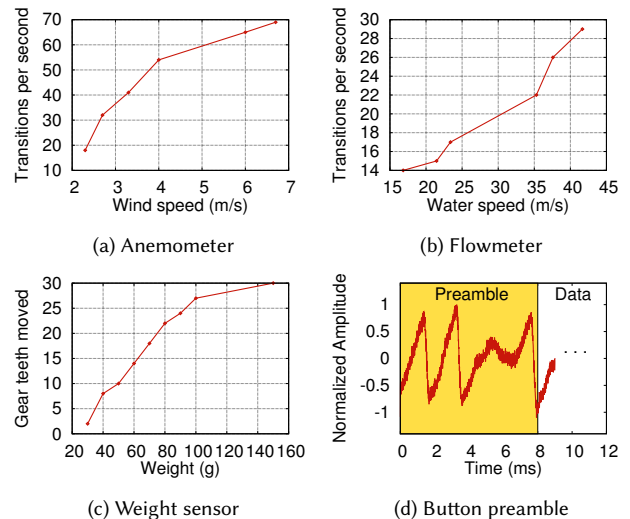


Fig. 23. (a)-(c) show the correlation for our 3D printed wireless sensors with ground truth measurements on the x-axis, (d) shows the backscattered signal corresponding to the preamble using the button prototype.

We vary the settings on a household fan to produce different wind speeds and measure the bit rate of the backscatter signal. The range of wind speeds that we were tested range from a World Meteorological Organization rating of “calm” to “gentle breeze” [Scale 2017] – designing for a wider range of wind speeds is not in the scope of this paper. We compare our bit rate measurements to ground truth from a commercial cup anemometer [Vaavud 2017]. Fig. 23(a) plots the number bit transitions versus increasing wind speed. The plot shows that as the wind speed increases, the number of bit transitions observed in the backscattered signal increases roughly linearly. This demonstrates that our 3D printed anemometer can wirelessly transmit the wind speed information using our backscatter design.

Wireless flowmeter. Flowmeters measure the velocity of moving fluids. Flowmeters are ideal IoT devices that can be installed onto any water pipe and used to collect analytics about water consumption in real time. Our flowmeter consists of a 3D printed rotor and a case which is connected to a backscatter gear as seen in Fig. 2. As before we use a gear with alternating sequences of zero and one bits. To evaluate our system we funnel water at different speeds from a tap into our flowmeter and record the rate of bit transitions.

Fig. 23(b) shows that as the speed of water increases, we see an increase in the number of bit transitions. Ground truth speed values were taken by measuring the amount of time taken for a water flow to fill a 500 mL container. We however note that this sensor design resulted in lower SNR due to the water leaking onto the antenna. We design an enclosure for our experimental setup to shield the antenna from water. Our backscatter measurements in Fig. 23(b) indicate a positive correlation with flow rate, thus demonstrating that our flowmeters can transmit their readings wirelessly.

Wireless weight scale. We design a scale that can measure weights ranging from 30 to 150g. As seen in Fig. 2, the weight sensor is comprised of a platform attached to a linear rack gear and a guide for the gear to slide through. When a weight is placed on the platform,



Fig. 24. Wi-Fi input widgets. (a) Button (b) Knob (c) Slider

the linear gear is depressed downward, rotates the backscatter gear and pushes against a coil spring. When the weight is lifted, the coil spring unravels and pushes the platform back up. We encode information using the number of gear teeth moved (i.e., bits). Fig. 23(c) shows that the number of bits linearly increases with the weight on the scale. Our output saturates at a weight of 150 g as the spring is fully coiled and cannot move further.

Wi-Fi input widgets. Next, we present 3D printed buttons, knobs and sliders using printed Wi-Fi that we build in Fig 24.

Wireless buttons. We design a button that automatically orders refills for common products, i.e., a 3D printed version of the Wi-Fi Amazon button. Each button uniquely encodes a product identifier using a coded gear in §3.1.3. The design of the button is similar to the weight scale. Specifically, we use a combination of linear and circular gears shown in Fig. 9(b). The gear is coupled to a spring that coils as the button is pressed, and then forces the rack back up to its original position when the force is removed. Thus, pushing the button drives a linear rack gear downwards, which then turns a coded gear to send data. Achieving data communication using push buttons requires us to address two unique challenges: 1) we need a mechanism to identify the beginning of a packet, and 2) since users can push buttons at different speeds, we need an algorithm for symbol synchronization. To address the second concern we use Manchester coding where a 1 bit is represented as the presence of a gear followed by its absence, while a 0 bit is represented as the absence of a gear followed by its presence. This ensures that any subsequence of bits has an equal number of zeros and ones, which allows us to synchronize the symbol boundaries. To determine the beginning of a packet transmission we design a four-gear sequence as a preamble. Specifically, we use two single gear teeth followed by a wider gear tooth equivalent to the length of two single teeth as shown in the gear in Fig. 8. Since this pattern does not occur within our data, we can use it to estimate the beginning of a bit sequence. Using our 24-tooth gear design, this leaves us 20 teeth for data transmission. With Manchester coding, this translates to 10 bits. Adding an additional 2 parity bits to account for bit errors resulting in 8 bits of data which can uniquely identify 256 products.

Wireless knobs and sliders. We create a knob that can sense rotational movement. The knob is attached to the backscatter gear. When the user rotates the knob, the receiver can infer the amount of rotation from the number of backscattered bits. We also create a slider shown in Fig. 24 that can sense linear movement. The slider is attached to a rack gear. Knobs and sliders can be used to enable rich physical interaction by sending information to a nearby Wi-Fi device with the user to control music volume and lights in a room. Further,



Fig. 25. 3D Printed Wi-Fi Smart Objects. (a) Tide bottle instrumented with a bolt-on flowmeter to track the amount of detergent remaining, and automatically order refills. (b) Test tube holder can be used for managing inventory and measuring the amount of liquid in each test tube.

since the sliders can encode different unique sets of bits, we can use multiple sliders in the same room to control different lights.

Wi-Fi smart objects. Finally, we present two different smart objects designed using printed Wi-Fi in Fig. 25.

Smart detergent bottle. Our smart bottle design detects when household supplies like detergent run low and requests refills via nearby Wi-Fi receivers. To address this, we design the bolt-on flowmeter in Fig. 25 that attaches to the cap of a detergent bottle and tracks how much detergent is used. The detergent that flows out of the bottle moves the flowmeter's rotor, which can be used to measure the flow of viscous substances like detergent.

Smart test tube rack. Our rack and pinion design can be used as pressure sensors for inventory tracking. We prototype a smart test tube rack for use in a wet lab to tell if a test tube is in the rack, and if so determine the amount of liquid present inside the tube based on its weight. Our design consists of an arm, which is connected to a gear rack and works similar to our wireless weight scale.

7 DISCUSSION AND CONCLUSION

This work is part of our long-term vision for democratizing the creation of IoT enabled objects that can communicate information seamlessly, everywhere and at anytime. 3D printed Internet connected devices are a key element of these future IoT devices with a wide range of applications including sensing, gaming, tracking, and robotics among many others. In this section, we discuss various aspects of our technology and outline avenues for future research.

Arbitrary surfaces. We incorporate the antenna for our Wi-Fi computational method on a narrow flat plane and incorporate the gears inside the desired object. We note that a large majority of objects have at least one planar surface, including the base. Further, the antenna can be incorporated just under the surface of an arbitrarily shaped object since plastic does not significantly attenuate Wi-Fi signals. Thus, our approach generalizes well to a wide set of objects. However, it is worthwhile exploring unconventional antenna designs that take advantage of the variety of geometrical 3d models.

Increased range. Our current usage model for printed Wi-Fi is for the user who is interacting the 3D printed object to carry the Wi-Fi receiver (e.g., smartphone) that can decode backscatter data. One can in principle use coding techniques to achieve much higher ranges.

Tracking and robotic applications. Since our printed Wi-Fi design is effectively generating radio signals, we can correlate the backscatter signal to track it in 3D and transform 3D printed objects into user interfaces. Printed Maglink can be beneficial for robotic applications where the embedded data can augment computer vision techniques to supply data about the shape and texture of target objects.

Acknowledgments. We thank the anonymous reviewers and Aaron Parks for helpful feedback on the paper. We thank Joshua Smith for help with the related work section. This work was funded in part by awards from the National Science Foundation, Sloan fellowship and Google Faculty Research Awards.

REFERENCES

- 3d Printing Industry. 2017. <https://3dprintingindustry.com/news/nanotech-pioneer-brings-3d-printable-metal-makers-91202/>. (2017).
- J. Adams, Eric. Duoss, T. Malkowski, M. Motala, B. Ahn, R. Nuzzo, J. Bernhard, and J. Lewis. 2011. Conformal printing of electrically small antennas on three-dimensional surfaces. *Advanced Materials* '11 (2011).
- G. Alemanno, P. Cignoni, N. Pietroni, F. Ponchio, and R. Scopigno. 2014. Interlocking Pieces for Printing Tangible Cultural Heritage Replicas.. In *Eurographics '14*.
- All3DP. 2017. 30 Types of 3D Printer Filament. <https://all3dp.com/best-3d-printer-filament-types-pla-abs-pet-exotic-wood-metal/>. (2017).
- M. Bächer, B. Hepp, F. Pece, P. Kry, B. Bickel, B. Thomaszewski, and O. Hilliges. 2016. Defsense: Computational design of customized deformable input devices. In *CHI-BarcodHQ*. 2017. <http://www.barcodhq.com/primer.html>. (2017).
- B. Bickel, P. Kaufmann, M. Skouras, B. Thomaszewski, D. Bradley, T. Beeler, P. Jackson, S. Marschner, W. Matusik, and M. Gross. 2012. Physical face cloning. *ACM Trans. Graph.* (July 2012), 118:1–118:10.
- J. Chan and S. Gollakota. 2017. Data Storage and Interaction using Magnetized Fabric. In Proceedings of the 30th Annual Symposium on User Interface Software and Technology (UIST '17). ACM.
- P. Deffenbaugh and K. Church. 2013. Fully 3D Printed 2.4 GHz Bluetooth/Wi-Fi Antenna. In *Symposium on Microelectronics* '13.
- Y. Dong, J. Wang, F. Pellacini, X. Tong, and B. Guo. 2010. Fabricating spatially-varying subsurface scattering. *ACM Trans. Graph.* (July 2010), 62:1–62:10.
- Electrifi. 2017. 100g Electrifi Conductive 3D Printing Filament. <https://www.multi3dlic.com/product/electrifi-3d-printing-filament/>. (2017).
- R. Fletcher and N. Gershenfeld. 2000. Remotely interrogated temperature sensors based on magnetic materials. In *IEEE transactions on magnetics '00*.
- R. Fletcher, J. Levitan, J. Rosenberg, and N. Gershenfeld. 1996. Application of smart materials to wireless ID tags and remote sensors. In *MRS Proceedings*.
- W. Gao, Y. Zhang, D. Nazzetta, K. Ramani, and R. Cipra. 2015. RevoMaker: Enabling Multi-directional and Functionally-embedded 3D Printing Using a Rotational Cuboidal Platform. In *UIST '15*.
- S. Gollakota, F. Adib, D. Katabi, and S. Seshan. 2011. Clearing the RF Smog: Making 802.11N Robust to Cross-technology Interference (SIGCOMM).
- C. Harrison, R. Xiao, and S. Hudson. 2012. Acoustic barcodes: passive, durable and inexpensive notched identification tags. In *UIST '12*.
- D. L. Hecht. 2001. Printed embedded data graphical user interfaces. In *IEEE Computer*.
- J. Hook, T. Nappey, S. Hodges, P. Wright, and P. Olivier. 2014. Making 3D Printed Objects Interactive Using Wireless Accelerometers. In *CHI EA '14*.
- W. Jiang, D. Ferreira, J. Ylioja, J. Goncalves, and V. Kostakos. 2014. Pulse: low bitrate wireless magnetic communication for smartphones. In *Ubicomp '14*.
- B. Kellogg, A. Parks, S. Gollakota, J. Smith, and D. Wetherall. 2014. Wi-fi Backscatter: Internet Connectivity for RF-powered Devices. In *SIGCOMM '14*.
- B. Kellogg, V. Talla, S. Gollakota, and J. Smith. 2016. Passive Wi-Fi: bringing low power to Wi-Fi transmissions. In *NSDI '16*.
- Y. Koyama, S. Sueda, E. Steinhardt, T. Igarashi, A. Shamir, and W. Matusik. 2015. AutoConnect: computational design of 3D-printable connectors. *ACM Trans. Graph.* (Oct. 2015), 231:1–231:11.
- Y. Lan, Y. Dong, F. Pellacini, and X. Tong. 2013. Bi-scale appearance fabrication. *ACM Trans. Graph.* (July 2013), 145:1–145:12.
- M. Lau, A. Ohgawara, J. Mitani, and T. Igarashi. 2011. Converting 3D furniture models to fabricatable parts and connectors. *ACM Trans. Graph.* (July 2011), 85:1–85:6.
- D. Li, D. Levin, W. Matusik, and C. Zheng. 2016. Acoustic Voxels: Computational Optimization of Modular Acoustic Filters. *ACM Trans. Graph.* (July 2016), 88:1–88:12.
- V. Liu, A. Parks, V. Talla, S. Gollakota, D. Wetherall, and J. Smith. 2013. Ambient Backscatter: Wireless Communication out of Thin Air. In *SIGCOMM '13*.
- R. MacCurdy, R. Katzschmann, Y. Kim, and D. Rus. 2015. Printable Hydraulics: A Method for Fabricating Robots by 3D Co-Printing Solids and Liquids. In *arXiv preprint*.
- B. Macq, P. Alface, and M. Montanola. 2015. Applicability of Watermarking for Intellectual Property Rights Protection in a 3D Printing Scenario. In *Web3D '15*.
- J. Martinez, J. Dumas, and S. Lefebvre. 2016. Procedural Voronoi Foams for Additive Manufacturing. *ACM Trans. Graph.* (July 2016), 44:1–44:12.
- Maxim. 2004. MAX2829/MAX2829 Single/Dual-Band 802.11a/b/g World-Band Transceiver ICs. <https://datasheets.maximintegrated.com/en/ds/MAX2828-MAX2829.pdf>. (2004).
- Y. Mori and T. Igarashi. 2007. Plushie: an interactive design system for plush toys. *ACM Trans. Graph.*, Article 45 (July 2007).
- F. Moshir and S. Singh. 2014. Wireless Barcodes for Tagging Infrastructure. In *MobiCom*.
- S. Mueller, S. Im, S. Gurevich, A. Teibrich, L. Pfisterer, F. Guimbretière, and P. Baudisch. 2014. WirePrint: 3D Printed Previews for Fast Prototyping. In *UIST '14*.
- Optomec. 2017. Optomec Internet of Things. <http://www.optomec.com/printed-electronics/aerosol-jet-core-applications/internet-of-things/>. (2017).
- H. Ota, S. Emaminejad, Y. Gao, A. Zhao, E. Wu, S. Challa, K. Chen, H. Fahad, A. Jha, D. Kiriya, et al. 2016. Application of 3D printing for smart objects with embedded electronic sensors and systems. In *AMT'16*.
- A. Parks, S. Gollakota, and J. Smith. 2014. Turbocharging ambient backscatter communication. In *SIGCOMM '14*.
- H. Peng, F. Guimbretière, J. McCann, and S. Hudson. 2016a. A 3D Printer for Interactive Electromagnetic Devices. In *UIST '16*.
- H. Peng, R. Wu, S. Marschner, and F. Guimbretière. 2016b. On-the-fly print: Incremental printing while modelling. In *CHI '16*.
- T. Pereira, S. Rusinkiewicz, and W. Matusik. 2014. Computational light routing: 3D printed optical fibers for sensing and display. *ACM Trans. Graph.* (July 2014), 24:1–24:13.
- S. Preradovic, I. Balbin, N. Karmakar, and G. Swiegers. 2009. Multiresonator-based chipless RFID system for low-cost item tracking. In *Microwave Theory and Techniques*.
- ProtoPasta. 2017. <https://www.proto-pasta.com/pages/magnetic-iron-pla>. (2017).
- V. Savage, S. Follmer, J. Li, and B. Hartmann. 2015a. Makers' Marks: Physical Markup for Designing and Fabricating Functional Objects. In *UIST '15*.
- V. Savage, A. Head, B. Hartmann, D. Goldman, G. Mysore, and W. Li. 2015b. Lamello: Passive acoustic sensing for tangible input components. In *CHI '15*.
- Beaufort Scale. 2017. <http://www.spc.noaa.gov/faq/tornado/beaufort.html>. (2017).
- M. Schmitz, M. Khalilbeigi, M. Balwierz, R. Lissermann, M. Mühlhäuser, and J. Steimle. 2015. Capricate: A Fabrication Pipeline to Design and 3D Print Capacitive Touch Sensors for Interactive Objects. In *UIST '15*.
- C. Schüller, D. Panizzo, A. Grundhöfer, H. Zimmer, E. Sorkine, and O. Sorkine-Hornung. 2016. Computational Thermoforming. *ACM Trans. Graph.*, 43:1–43:9.
- C. Schumacher, B. Bickel, J. Rys, S. Marschner, C. Daraio, and M. Gross. 2015. Microstructures to control elasticity in 3D printing. *ACM Trans. Graph.* (July 2015), 136:1–136:13.
- W. Su, R. Bahr, S. A. Nauroze, and M. M. Tentzeris. 2016. 3D printed reconfigurable helical antenna based on microfluidics and liquid metal alloy. In *IEEE International Symposium on Antennas and Propagation*.
- V. Subramanian, P. C. Chang, J. B. Lee, S. E. Molesa, D. R. Redinger, and S. K. Volkman. 2006. All-printed RFID tags: Materials and circuit implications. In *VLSID'06*.
- Z. Sun and I. F. Akyildiz. 2010. Magnetic Induction Communications for Wireless Underground Sensor Networks. In *IEEE Transactions on Antennas and Propagation*.
- Tedpella. 2017. https://www.tedpella.com/semmisc_html/sempaint.htm. (2017).
- David Tse and Pramod Viswanath. 2005. *Fundamentals of Wireless Communication*. Cambridge University Press, USA.
- F. Ucccheddu, M. Corsini, and M. Barni. 2004. Wavelet-based Blind Watermarking of 3D Models. In *Multimedia and Security '04*.
- Vaavud. 2017. Vaavud. <https://vaavud.com/>. (2017).
- M. Vázquez, E. Brockmeyer, R. Desai, C. Harrison, and S. Hudson. 2015. 3D Printing Pneumatic Device Controls with Variable Activation Force Capabilities. In *CHI '15*.
- A. Wang, V. Iyer, V. Talla, J. Smith, and S. Gollakota. 2017. Making Everyday Objects into FM Radio Stations. In *NSDI '17*.
- L. Wang and E. Whiting. 2016. Buoyancy optimization for computational fabrication. In *Eurographics '16*.
- K. Willis, E. Brockmeyer, S. Hudson, and I. Poupyrev. 2012. Printed Optics: 3D Printing of Embedded Optical Elements for Interactive Devices. In *UIST '12*.
- K. Willis and A. Wilson. 2013. InfraStructs: Fabricating Information Inside Physical Objects for Imaging in the Terahertz Region. *ACM Trans. Graph.* (July 2013), 138:1–138:10.
- S. Wu, C. Yang, W. Hsu, and L. Lin. 2015. 3D-printed microelectronics for integrated circuitry and passive wireless sensors. In *Microsystems & Nanoengineering '15*.
- S. Yamazaki, S. Kagami, and M. Mochimaru. 2014. Extracting watermark from 3D prints. In *ICPR '14*.
- B. Yeo and M. Yeung. 1999. Watermarking 3D objects for verification. In *IEEE Computer Graphics and Applications '99*.
- Zebra. 2017. RFID. <https://www.zebra.com/us/en/products/printers/rfid.html>. (2017).
- P. Zhang, M. Rostami, P. Hu, and D. Ganesan. 2016. Enabling practical backscatter communication for on-body sensors. In *SIGCOMM '16*.